PHYSICAL REVIEW A **102**, 023305 (2020)

Phase separation of a Bose-Bose mixture: Impact of the trap and particle-number imbalance

Maxim Pyzh[1,*] and Peter Schmelcher[1,2,†]
[1]*Zentrum für Optische Quantentechnologien, Universität Hamburg, Luruper Chaussee 149, 22761 Hamburg, Germany*
[2]*The Hamburg Centre for Ultrafast Imaging, Universität Hamburg, Luruper Chaussee 149, 22761 Hamburg, Germany*

(Received 16 May 2020; accepted 14 July 2020; published 5 August 2020)

We explore a few-body mixture of two bosonic species confined in quasi-one-dimensional parabolic traps of different length scales. The ground-state phase diagrams in the three-dimensional parameter space spanned by the harmonic length scale ratio, interspecies coupling strength, and particle-number ratio are investigated. As a first case study we use the mean-field ansatz (MF) to perform a detailed analysis of the separation mechanism. It allows us to derive a simple and intuitive rule predicting which of the immiscible phases is energetically more favorable at the miscible-immiscible phase boundary. We estimate the critical coupling strength for the miscible-immiscible transition and perform a comparison to correlated many-body results obtained by means of the multilayer multiconfiguration time-dependent Hartree method for bosonic mixtures (ML-X). At a critical ratio of the trap frequencies, determined solely by the particle-number ratio, the deviations between MF and ML-X are very pronounced and can be attributed to a high degree of entanglement between the components. As a result, we evidence the breakdown of the effective one-body picture. Additionally, when many-body correlations play a substantial role, the one-body density is in general not sufficient for deciding upon the phase at hand which we demonstrate exemplarily.

DOI: 10.1103/PhysRevA.102.023305

I. INTRODUCTION

Binary mixtures of ultracold gases have been extensively studied over the past years. They represent a unique platform for the investigation of complex interacting many-body quantum systems in a well-controlled environment. In particular, it is experimentally possible to shape the geometry of the trap [1], to reduce the dimensionality of the relevant motion [2,3], to tune the interparticle interactions [4–8], and prepare samples of only a few atoms [9,10]. Numerous experiments have been conducted with different hyperfine states [11–24], different elements [25–38], or different isotopes [39,40] to reveal how the interplay between two condensates impacts their stationary properties and nonequilibrium dynamics. Highlights of these explorations include among others the phase separation between the components and symmetry-breaking phenomena [12,17,36,37,39], the observation of Efimov physics [38], and creation of deeply bound dipolar molecules [28,32,33], as well as dark-bright solitary waves [18,19] and quantum droplets [23,24].

One of the key properties, which makes the multicomponent systems attractive and their physics very rich, is the miscibility, which has significant implications for sympathetic cooling [15,26], coarse-graining dynamics [41–44], and vortex formation [45,46], to name a few. In the very early theoretical investigations a very rich phase space for the ground state of the Bose-Bose mixture has been identified. These investigations [47–52] are based on the one-body densities obtained from solving the underlying mean-field equations, commonly known as Gross-Pitaevskii equations. In case of a weak intercomponent coupling one finds a miscible phase with a high spatial overlap between the components. For a sufficiently large repulsive coupling there are three types of segregated phases with a rather small overlap. Two of them are core-shell phases with one component being symmetrically surrounded by the other component, whereas the third is an asymmetrical phase, where the rotational or parity symmetry of the underlying trapping potential is broken. Neglecting the kinetic energy (Thomas-Fermi approximation), a simple separation criterion for the miscible-immiscible transition has been derived [53–55]. It depends solely on the intraspecies and interspecies interaction strengths, which are easily adjustable by Feshbach or confinement-induced resonances [4–8].

However, it has been shown that this separation criterion, while valid in homogeneous systems, should be applied with care in inhomogeneous geometries. Thus, in a harmonic confinement, system parameters such as trap frequency, particle numbers, and mass ratio have also an impact on the miscible-immiscible phase boundary [56–60]. The miscibility of a binary mixture of both bosons and fermions has been recently addressed also in other trapping geometries, i.e., in a box [61], double well [62–64], ring lattice [65–67], and combinations thereof [68], as well as the dynamical aspect of phase separation leading to pattern formations [69–72]. From the intuitive point of view, the trap pressure favors miscibility since it costs energy to extend in space. Thus, it requires stronger intercomponent repulsion for the species to separate. However, there are still open questions regarding the impact of different length scales, the characterization of boundaries

---

[*] mpyzh@physnet.uni-hamburg.de
[†] pschmelc@physnet.uni-hamburg.de

between the immiscible phases, and what type of separation will occur once the critical coupling is reached.

Another relevant topic affecting the critical coupling strength for a transition as well as the resulting type of phase are the interspecies correlations, which generate entanglement between the components and lead to bunching of particles of the same species. Although a mean-field treatment is often justified in experimental setups, a very thorough numerical analysis of one-dimensional (1D) few-body systems has revealed that an asymmetric immiscible phase is one of the two possible configurations of an entangled many-body state, the other one being the mirror image. The one-body densities of this so-called composite fermionization phase [73–77] preserve parity symmetry of the underlying trapping potential and have a high spatial overlap, which is uncharacteristic for an immiscible phase. Nevertheless, the components are indeed separated, which is encoded in the interspecies two-body density matrix. In experiments, the single shots do not represent one-body densities but are projections on one of the two mutually exclusive configurations. An averaging procedure would reveal a parity-preserving density, unless the Hamiltonian itself violates that symmetry, such as not coinciding trap centers of the one-body potentials. Apart from composite fermionization, there are a whole class of so-called spin-chain phases with an even higher degree of entanglement [78–80]. When all interactions in the system become nearly resonant, many states become quasidegenerate and particles, being bosons, gain fermionic features like the Pauli exclusion principle.

Considering the above, our work addresses three different points. First, we characterize the phase diagram in a three-dimensional parameter space spanned by the ratio of the harmonic trap lengths, the interspecies coupling strength, and the particle-number ratio. We switch off intracomponent interactions to reduce the complexity and gain a better understanding of the separation process. A very rich phase diagram is revealed admitting two tricritical points, where three phases may coexist. Second, within the framework of a mean-field approximation, we perform a detailed analysis of the separation mechanism. Equipped with this knowledge we derive a selection rule for phase separation processes and a simple algorithm to estimate the miscible-immiscible phase boundary. Finally, we investigate the deviations of the mean-field picture to a many-body approach. For this we use the multilayer multiconfiguration time-dependent Hartree method for bosonic mixtures [81–83]. We find that in the vicinity of the high-entanglement regime the phase diagram is indeed greatly affected. The symmetry-broken phase is replaced by the composite fermionization, while the onset of symmetry breaking is linked to the degree of entanglement reaching a certain threshold. Furthermore, the location of this beyond-mean-field regime strongly depends on the harmonic length scale ratio and the particle-number ratio. We also find that the one-body density is in general not sufficient to distinguish between a core-shell phase and the composite fermionization.

This work is organized as follows. In Sec. II we introduce our physical setup and in Sec. III our computational approach. Section IV is dedicated to a detailed study of a few-body mixture. Section IV A provides intuitive insights in the framework of the mean-field approximation, while Sec. IV B focuses on correlation and entanglement effects using multilayer multiconfiguration time-dependent Hartree method for bosonic mixtures. The few-to-many-body transition is subject of Sec. V. Finally, we summarize our findings in Sec. VI.

II. GENERAL FRAMEWORK

Our system consists of a particle-imbalanced mixture of two distinguishable bosonic components, denoted by $\sigma \in \{M, I\}$, with N_M particles in the majority component and N_I impurities. All particles are assumed to be of equal mass m and the intracomponent interactions are assumed to be zero or negligibly small. The majority species interacts with the impurities via s-wave contact interaction of coupling strength g_{MI}. The species are confined in separate quasi-1D harmonic traps of different length scales $a_\sigma = \sqrt{\hbar/m\omega_\sigma}$ with trap frequency ω_σ and coinciding trap centers. By choosing a_M and $\hbar\omega_M$ as length and energy scales we arrive at the rescaled Hamiltonian:

$$\begin{aligned} H &= H_M + H_I + H_{MI} \\ &= \sum_{i=1}^{N_M} \left(-\frac{1}{2}\frac{\partial^2}{\partial x_i^2} + \frac{1}{2}x_i^2 \right) + \sum_{i=1}^{N_I} \left(-\frac{1}{2}\frac{\partial^2}{\partial y_i^2} + \frac{1}{2}\eta^2 y_i^2 \right) \\ &\quad + g_{MI} \sum_{i=1}^{N_M} \sum_{j=1}^{N_I} \delta(x_i - y_j), \end{aligned} \tag{1}$$

where x_i labels the spatial coordinate of the ith majority particle, y_i of the ith impurity particle, and $\eta = \omega_I/\omega_M$ denotes the trap frequency ratio.

In this work we focus on the ground-state characterization and consider both attractive and repulsive interactions ranging from weak to intermediate couplings $g_{MI} \in [-2, 2]$ with the impurity being localized or delocalized with respect to the majority species, i.e., $a_I/a_M = \sqrt{1/\eta} \in [0.5, 1.5]$. We also study the impact of the particle-number ratio N_I/N_M on the system's properties concentrating on a few-body system.

All the ingredients necessary for the realization of such a Hamiltonian system have been demonstrated experimentally. Mixtures of two-component BECs with the same mass can be prepared with different atomic spin states [11–24]. The 1D geometry can be achieved by strong transversal confinement or by a two-dimensional optical lattice. The interaction strengths are tunable by Feshbach and confinement-induced resonances allowing to vary the coupling strength between the components and to make the intracomponent interactions negligible [4–8]. Species-dependent trapping techniques have been demonstrated [84,85]. Few-body systems are obtainable for fermions via trap spilling [86] and for bosons by cutting out a subsystem of a Mott insulator [87]. High-resolution measurements with single-atom sensitivity have been proposed for nonlattice traps by using a quantum gas microscope [88]. The experimental realization, however, has yet to be demonstrated.

III. COMPUTATIONAL APPROACH

To find the ground state of our binary mixture, we employ imaginary-time propagation by means of the multilayer multiconfigurational time-dependent Hartree method for atomic mixtures (ML-MCTDHX). For reasons of brevity we call it

ML-X from now on. This multiconfigurational wave-function-based method for efficiently solving the time-dependent Schrödinger equation was first developed for distinguishable degrees of freedom [89] and ML-X is an extension to indistinguishable particles such as bosons or fermions and mixtures thereof [81–83]. ML-X is an *ab initio* method, whose power lies in expanding the wave function in time-dependent basis functions. Let us demonstrate the underlying ansatz for the system at hand:

$$|\Psi(t)\rangle = \sum_{i=1}^{S} \sqrt{\lambda_i(t)}\, \left|\Psi_i^M(t)\right\rangle \otimes \left|\Psi_i^I(t)\right\rangle, \tag{2}$$

$$\left|\Psi_i^\sigma(t)\right\rangle = \sum_{\vec{n}^\sigma|N_\sigma} C_{i,\vec{n}^\sigma}(t)\, |\vec{n}^\sigma(t)\rangle\, . \tag{3}$$

The time-dependent many-body wave function $|\Psi(t)\rangle$ has two layers: the so-called species layer (2) and the particle layer (3). In the first step (2) we separate majority and impurity species and assign them to $S \in \mathbb{N}$ corresponding species wave functions $|\Psi_i^\sigma(t)\rangle$. The time-dependent coefficients $\lambda_i(t)$ are normalized $\sum_{i=1}^{S} \lambda_i(t) = 1$ and describe the degree of entanglement between the components. In case $\exists\ i \in \{1, \dots, S\} : \lambda_i(t) \approx 1$ the components are said to be disentangled. In the second step (3) each species wave function $|\Psi_i^\sigma(t)\rangle$, which depends on N_σ indistinguishable coordinates, is expanded in terms of species-dependent symmetrized product states, also known as permanents or number states $|\vec{n}^\sigma\rangle = |n_1^\sigma, \dots, n_{s_\sigma}^\sigma\rangle$ admitting $s_\sigma \in \mathbb{N}$ normalized single-particle functions (SPF) $|\varphi_j^\sigma(t)\rangle$. The sum is over all possible configurations $\vec{n}^\sigma|N_\sigma$ fulfilling the constraint $\sum_{i=1}^{s_\sigma} n_i^\sigma = N_\sigma$. The time dependence of number states is meant implicitly through the time dependence of the underlying SPFs. Finally, each SPF is represented on a primitive one-dimensional time-independent grid [90].

When one applies the Dirac-Frenkel variational principle [91] to the above ansatz, one obtains coupled equations of motion for the expansion coefficients $\lambda_i(t)$, $C_{i,\vec{n}^\sigma}(t)$ and the SPFs $|\varphi_j^\sigma(t)\rangle$. This procedure allows to considerably reduce the size of the basis set as compared to choosing time-independent SPFs constituting the number states on the particle layer (3). We note that $S = 1 \wedge s_\sigma = 1$ is equivalent to solving coupled Gross-Pitaevskii equations. We will show parameter regions, where the mean-field description is valid and regions where it fails as a result of increasing interspecies correlations. These generate entanglement between the components and decrease the degree of condensation of the noninteracting majority atoms.

The results of the ML-X calculations are considered to be converged if two criteria are simultaneously satisfied. First, the expansion coefficients λ_i on the species layer as well as populations of the natural orbitals m_i^σ [1] of species σ on the particle layer feature an exponential decay[2] as a function of the number of orbitals. This ensures that every newly added orbital or SPF adds a significantly smaller correction to the many-body wave function. Second, the smallest coefficients $\lambda_S < \epsilon$ and $m_{s_\sigma}^\sigma < \epsilon$ are below some threshold value ϵ. The value of ϵ depends in general on the observable of interest and ensures that the least contributing orbital or SPF does only a minor correction to the observable. The ML-X simulations obtained in this work are converged in the above sense with $\epsilon = 10^{-3}$ unless stated otherwise.

In the following, we will often refer to the one-body density $\rho_1^\sigma(z)$ of species σ, two-body density matrix $\rho_2^\sigma(z, z')$ of species σ, and interspecies two-body density matrix $\rho_2^{MI}(x, y)$ of the many-body density operator $\hat{\rho} = |\Psi\rangle\langle\Psi|$ defined as

$$\rho_1^\sigma(z) \ = \langle z|\, \mathrm{tr}_{N_\sigma\setminus 1}\left\{\mathrm{tr}_{N_{\bar{\sigma}}}\{\hat{\rho}\}\right\} |z\rangle\, , \tag{4}$$

$$\rho_2^\sigma(z, z') \ = \langle z, z'|\, \mathrm{tr}_{N_\sigma\setminus 2}\left\{\mathrm{tr}_{N_{\bar{\sigma}}}\{\hat{\rho}\}\right\} |z, z'\rangle\, , \tag{5}$$

$$\rho_2^{MI}(x, y) \ = \langle x, y|\, \mathrm{tr}_{N_M\setminus 1}\left\{\mathrm{tr}_{N_I\setminus 1}\{\hat{\rho}\}\right\} |x, y\rangle\, , \tag{6}$$

where $N_\sigma \setminus n$ stands for integrating out $N_\sigma - n$ coordinates of component σ and $\bar{\sigma} \neq \sigma$.

IV. PHASE SEPARATION: FEW-BODY MIXTURE

We start our analysis with a few-body system consisting of $N_M = 5$ majority particles with $N_I \in \{1, 2\}$ impurities. In Sec. V we will discuss cases with larger particle imbalance. Since we aim at the comparison between the mean-field approximation and a many-body approach, we can ensure reasonably converged results only for relatively small system sizes. As we have emphasized previously in Sec. II, such few-body systems are experimentally accessible.

The outline is as follows. First, in Sec. IV A, we obtain the phase diagram within the mean-field approximation. We uncover the mechanism responsible for the phase separation by using an effective description and apply the obtained intuition to derive an estimate for the miscible-immiscible phase boundary. Second, in Sec. IV B, we perform a comparison to the correlated many-body treatment by means of ML-X. Apart from visible changes in the phase diagram we identify the parameter space with a quick buildup of the entanglement reaching large values already for moderate couplings. We then develop an understanding how our intuitive one-body picture is altered due to the presence of entanglement and what implications it has for the ground-state phases, in particular in the parameter space with considerable entanglement.

A. Mean-field approach: Basic mechanism of phase separation

For the mean-field description we choose a single species orbital $S = 1$, yielding a nonentangled state $|\Psi(t)\rangle = |\Psi^M(t)\rangle \otimes |\Psi^I(t)\rangle$ on the species layer. On the particle layer a single SPF $s_\sigma = 1$ is used for each component, meaning that particles of the same species are forced to condense into the same single-particle state $\varphi^\sigma(z, t)$ and $|N_\sigma\rangle$ is the only possible number state on the particle level. Thus, our ansatz is $|\Psi(t)\rangle = |N_M(t)\rangle \otimes |N_I(t)\rangle$ and only $\varphi^\sigma(z, t)$ are time dependent. As a result of imaginary-time propagation, we end up with the ground-state orbitals $\varphi_{\mathrm{MF}}^\sigma(z)$. The interpretation of the mean-field treatment is that each species feels in addition to its own external potential an averaged one-body potential

---

[1] In the spectral decomposition of the one-body density operator $\hat{\rho}_1^\sigma = \sum_{i=1}^{s_\sigma} m_i^\sigma\, |m_i^\sigma\rangle\langle m_i^\sigma|$ the m_i^σ are called natural populations and $|m_i^\sigma\rangle$ natural orbitals.

[2] λ_i and m_i^σ are sorted by magnitude in descending order.

induced by the other component. To obtain the effective mean-field Hamiltonian H_σ^{MF} of species σ we need to integrate out the other component $\bar{\sigma}$. For convenience, we also subtract the energy offset $c_{\bar{\sigma}} = \langle N_{\bar{\sigma}}|H_{\bar{\sigma}}|N_{\bar{\sigma}}\rangle$ caused by the one-body energy of component $\bar{\sigma}$:

$$\begin{aligned} H_\sigma^{\mathrm{MF}} &= \langle N_{\bar{\sigma}}|H|N_{\bar{\sigma}}\rangle - c_{\bar{\sigma}} \\ &= H_\sigma + N_{\bar{\sigma}} g_{MI} \sum_{i=1}^{N_\sigma} \rho_{MF}^{\bar{\sigma}}(z_i) \\ &= \sum_{i=1}^{N_\sigma} \left(-\frac{1}{2}\frac{\partial^2}{\partial z_i^2} + V_\sigma(z_i) + V_\sigma^{\mathrm{ind}}(z_i) \right) \\ &= \sum_{i=1}^{N_\sigma} \left(-\frac{1}{2}\frac{\partial^2}{\partial z_i^2} + V_\sigma^{\mathrm{eff}}(z_i) \right), \end{aligned} \tag{7}$$

where $\rho_{\mathrm{MF}}^\sigma(z) = |\varphi_{\mathrm{MF}}^\sigma(z)|^2$ is the one-body density of species σ normalized as $\int dz\, \rho_{\mathrm{MF}}^\sigma(z) = 1$, $V_\sigma^{\mathrm{ind}}(z) = N_{\bar{\sigma}} g_{MI} \rho_{\mathrm{MF}}^{\bar{\sigma}}(z)$ the induced one-body potential, $V_\sigma^{\mathrm{eff}}(z) = V_\sigma(z) + V_\sigma^{\mathrm{ind}}(z)$ the effective one-body potential and $\bar{\sigma} \neq \sigma$.

To systematically distinguish between different phases, we define the following two functions, applicable also in the more general case of a many-body treatment in Sec. IV B:

$$\Delta_\sigma = \frac{\rho_1^\sigma(z=0)}{\max_z \rho_1^\sigma(z)}, \tag{8}$$

$$d = \left| \int_{-\infty}^{\infty} dz\, z \rho_1^M(z) - \int_{-\infty}^{\infty} dz\, z \rho_1^I(z) \right|, \tag{9}$$

with the one-body density $\rho_1^\sigma(z)$ of component σ (4). Equation (8) compares the one-body density $\rho_1^\sigma(z)$ at the trap center with its maximum value, while Eq. (9) checks for parity asymmetry, as we will argue below. The above equations are motivated from the literature on binary mixtures and we provide a brief summary on the discovered ground-state phases and some of their properties, which will be relevant in the following discussions.

For weak couplings there is a miscible phase M with a high spatial overlap of the one-body densities $\rho_1^\sigma(z)$. As a result, both components exhibit a Gaussian profile ($\Delta_\sigma = 1$) and occupy the center of their trap ($d = 0$). The state is disentangled and both species are condensed. For negative couplings, i.e., attractive interactions, the phase remains miscible and the widths of the Gaussian densities shrink with decreasing coupling strength. For stronger positive couplings, three different phase separation scenarios are possible. In case the majority species occupies the trap center ($\Delta_M = 1$), pushing the impurities outside in a way that the impurity density forms a shell around the majority density with two parity-symmetric humps ($\Delta_I < 1$ and $d = 0$), we have a core-shell IMI phase. When the impurities remain at the trap center instead ($\Delta_I = 1$) with the majority species forming a shell ($\Delta_M < 1$ and $d = 0$), we have a core-shell MIM phase. Finally, when both species develop two parity-symmetric humps with a local minimum at the trap center ($\Delta_\sigma < 1$ and $d = 0$), we have a composite fermionization phase CF. On the level of one-body densities CF appears to be miscible owing to the high spatial overlap between the components. However, the deviations to the miscible phase become evident upon investigating the two-body density matrices (5) and (6). Namely, two particles of the same component can be found either on the left or the right side with respect to trap center, while two particles of different components are always on opposite sides.

While the core-shell phases IMI and MIM do not rely on entanglement between the components, CF is always an entangled many-body state made out of two major species orbitals $S = 2$ and two major SPFs $s_\sigma = 2$ on the particle layer. Thus, CF cannot be obtained within the mean-field approximation. In fact, we observe that once the entanglement of the true many-body state, characterized by the von Neumann entropy (see Sec. IV B), reaches a certain threshold, a collapse to a phase with broken parity symmetry ($d > 0$) will take place in the mean-field picture. We abbreviate this phase with SB from now on.

The origin of SB is the onset of a quasidegeneracy between the ground state and the first excited state of the many-body spectrum, which becomes an exact degeneracy in the limit of $g_{MI} \to \infty$. Once this limit is reached, any superposition of those two states is also an eigenstate of (1). Since they are of different parity symmetry P and $[H, P] = 0$, it is possible to choose the superposition to be parity symmetric or to break the parity symmetry of (1). It was suggested [73] that the corresponding many-body wave function may be written in terms of number states as $|\Psi\rangle = c_1\, |N_M\rangle_L\, |0_M\rangle_R \otimes |0_I\rangle_L\, |N_I\rangle_R + c_2\, |0_M\rangle_L\, |N_M\rangle_R \otimes |N_I\rangle_L\, |0_I\rangle_R$ with two parity-broken SPFs $\varphi_j^\sigma(z)$ featuring an asymmetric Gaussian shape with a maximum on the $j = L$ (left) or $j = R$ (right) side with respect to the trap center. Within the mean-field approximation, the eigenenergy of the first excited state coincides with the ground-state energy already for a finite coupling g_{MI}. Since mean field does not incorporate entanglement, the state collapses either to $|N_M\rangle_L \otimes |N_I\rangle_R$ or to $|N_M\rangle_R \otimes |N_I\rangle_L$, resulting in a phase with broken parity symmetry.

With this we end our overview over different phases and showcase a compact summary of the phases:

$$\begin{cases} M & : d = 0 \wedge \Delta_M = 1 \wedge \Delta_I = 1, \\ IMI & : d = 0 \wedge \Delta_M = 1 \wedge \Delta_I < 1, \\ MIM & : d = 0 \wedge \Delta_M < 1 \wedge \Delta_I = 1, \\ CF & : d = 0 \wedge \Delta_M < 1 \wedge \Delta_I < 1, \\ SB & : d > 0 \wedge \Delta_M < 1 \wedge \Delta_I < 1. \end{cases} \tag{10}$$

In Fig. 1 we depict the ground-state phases within the mean-field approximation for $N_B = 5$ with (a) $N_I = 1$ and (b) $N_I = 2$ impurities as a function of the intercomponent coupling strength g_{MI} and the impurity localization a_I/a_M. As expected, CF is not among the phases in Fig. 1. The transition region on the a_I/a_M axis, where core shell MIM is replaced by core shell IMI, can be tuned by variation of the particle-number ratio such that for $N_I = N_M$ it lies at $a_I/a_M = 1$ (not shown), while for increasing particle imbalance $N_I/N_M < 1$ it is shifted toward a lower a_I/a_M ratio. This is also the point where the coupling strength g_{MI}, required for the realization of the SB phase, is the smallest. We will see later in Sec. IV B that the species entropy has here its global maximum. Note that each phase diagram features critical points, where three different phases can coexist (green circles).

Now that we have identified the phases, we are going to shed some light on the mechanism behind the phase separation taking place for different specific coupling strength g_{MI} for

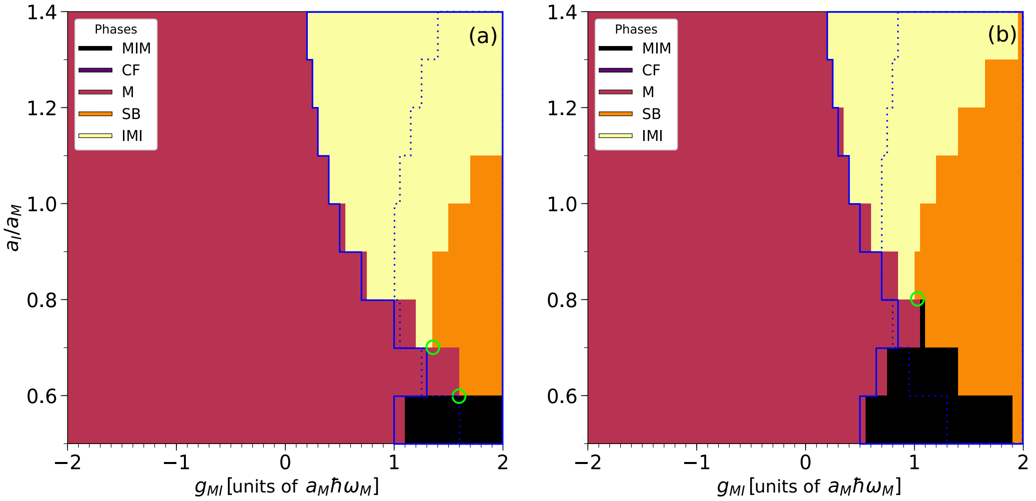

FIG. 1. Mean-field ground-state phase diagram for $N_B = 5$ majority particles and (a) $N_I = 1$ or (b) $N_I = 2$ impurities as a function of the intercomponent coupling strength g_{MI} and impurity localization $a_I/a_M = \sqrt{1/\eta}$ with $\eta = \omega_I/\omega_M$ being the trap frequency ratio and $a_\sigma = \sqrt{\hbar/m\omega_\sigma}$ the harmonic oscillator length of species σ. The nomenclature of phases is as follows: *M* for miscible, *MIM* for core shell with impurity at the core, *IMI* for core shell with majority at the core, *CF* for composite fermionization, and *SB* for a phase with broken parity symmetry. The blue solid curve represents the miscible-immiscible phase boundary according to (19). The blue dotted line is an estimate for the *SB* phase boundary according to (21). Green circles indicate tricritical points. The coarse structure is due to the finite step size of our data with respect to a_I/a_M.

a fixed trap ratio η. In particular, we will provide a simple formula, which determines which of the core-shell structures is energetically more favorable. Additionally, we provide an estimate on the miscible-immiscible transition region and on the *SB* phase boundary.

Let us make two horizontal cuts across the phase diagram of Fig. 1(b) at $a_I/a_M = 0.5$ and at $a_I/a_M = 1.1$. In Fig. 2 we take a closer look at the variation of the one-body densities ρ^σ_{MF} being part the effective one-body potential V^{eff}_σ (7) when increasing the coupling strength g_{MI}. First, let us focus on

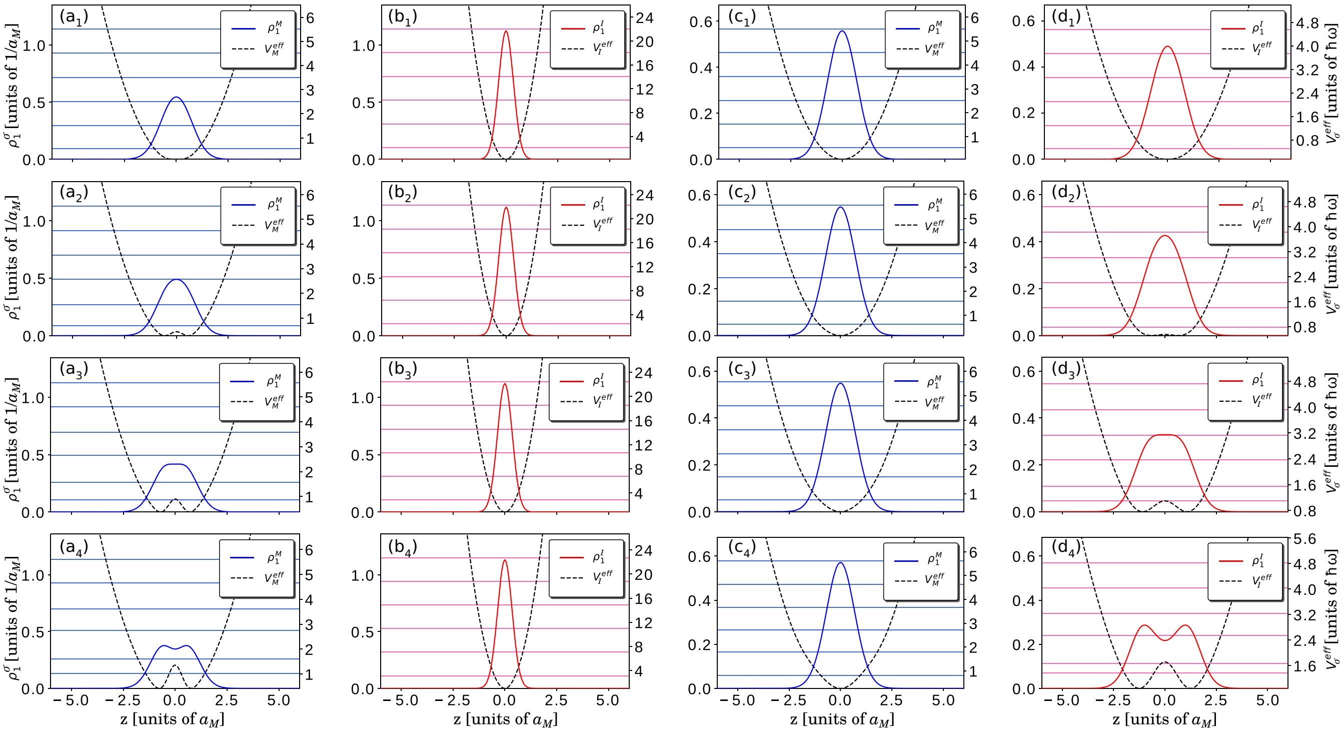

FIG. 2. Ground-state densities $\rho^\sigma_{\text{MF}}(z)$ inside the induced one-body potential $V^{\text{eff}}_\sigma(z)$ from (7) for $N_M = 5$, $N_I = 2$ and either $a_I/a_M = 0.5$ (columns 1 and 2 for majority and impurity species, respectively) or $a_I/a_M = 1.1$ (columns 3 and 4 for majority and impurity species, respectively). Rows from top to bottom correspond to a variation of the intercomponent coupling $g_{MI} \in \{0.05, 0.2, 0.4, 0.6\}$. Horizontal lines depict eigenenergies of (7).

columns 1 and 2, corresponding to $a_I/a_M = 0.5$. For very weak coupling (first row), every atom to a good approximation populates the energetically lowest harmonic oscillator orbital of the respective potential V_σ. The induced potential V_σ^{ind} gains an amplitude linearly with g_{MI} and with the density profiles being Gaussians of different widths we observe the appearance of a small barrier in V_M^{eff} at $g_{MI} = 0.2$ [Fig. 2(a2)]. This barrier grows with g_{MI} and at $g_{MI} = 0.4$ [Fig. 2(a3)] it becomes comparable to the ground-state energy of the effective potential, while the one-body density ρ_{MF}^M turns flat at the trap origin. Once the ground-state energy drops below the barrier height, two density humps appear and core shell *MIM* is established [Fig. 2(a4)]. Meanwhile, the effective potential of the impurity V_I^{eff} does not show significant deviations from the harmonic case (second column). Especially, the induced part V_I^{ind}, being initially also a Gaussian, is not capable to produce a barrier at the trap center. Similar statements can be made for columns 3 and 4, corresponding to $a_I/a_M = 1.1$. The only difference is that V_I^{eff} develops a barrier instead, whereas V_M^{eff} shows only a slight variation, which finally leads to the core-shell *IMI* phase.

Motivated by the above observation, we define an alternative phase classification from an energetical point of view:

$$\begin{cases} M & : E_{0,\sigma}^{\text{MF}} - V_\sigma^{\text{eff}}(0) > 0, \\ IMI & : E_{0,M}^{\text{MF}} - V_M^{\text{eff}}(0) > 0 \ \wedge \ E_{0,I}^{\text{MF}} - V_I^{\text{eff}}(0) < 0, \\ MIM & : E_{0,M}^{\text{MF}} - V_M^{\text{eff}}(0) < 0 \ \wedge \ E_{0,I}^{\text{MF}} - V_I^{\text{eff}}(0) > 0, \\ SB & : d > 0, \end{cases} \tag{11}$$

where $E_{0,\sigma}^{\text{MF}}$ is the ground-state energy of (7). As long as the ground-state energy of the effective species Hamiltonian exceeds the effective potential height at the trap center, the species remains at the trap center. Phase diagrams produced this way match exactly the ones shown in Fig. 1.

The interpretation is now as follows. For a very weak coupling, both the majority and the impurity reside in the ground state of the harmonic oscillator. Once the induced potential V_σ^{ind} of species σ becomes large enough to produce a barrier in V_σ^{eff}, the corresponding density ρ_{MF}^σ will start to expand. By growing in width it will prevent the other component $\bar{\sigma}$ from developing a barrier of its own. When the height of the potential barrier becomes of the same magnitude as the lowest energy of the corresponding effective potential, the species σ splits into two fragments. Then, it starts squeezing the other component $\bar{\sigma}$ by increasing the effective trap frequency of the renormalized harmonic oscillator $V_{\bar{\sigma}}^{\text{eff}}$.

The barrier in V_σ^{eff} appears once the following condition is fulfilled:

$$\exists\, x_0 \neq 0 : \frac{d}{dx} V_\sigma^{\text{eff}}\Big|_{x_0} = 0. \tag{12}$$

Assuming one-body densities to be unperturbed harmonic oscillator ground states, we obtain the following effective potentials:

$$V_M^{\text{eff}}(z) \approx \frac{1}{2} z^2 + g_{MI} N_I \sqrt{\frac{\eta}{\pi}} e^{-\eta z^2}, \tag{13}$$

$$V_I^{\text{eff}}(z) \approx \frac{1}{2} \eta^2 z^2 + g_{MI} N_M \sqrt{\frac{1}{\pi}} e^{-z^2}, \tag{14}$$

and the corresponding barrier conditions

$$\frac{\sqrt{\pi}}{2 N_I \sqrt{\eta^3}} \mathrel{\hat{=}} g_{MI}^M < g_{MI}, \tag{15}$$

$$\frac{\sqrt{\pi}\eta^2}{2 N_M} \mathrel{\hat{=}} g_{MI}^I < g_{MI}. \tag{16}$$

For given particle numbers N_M, N_I and trap ratio η either condition (15) or condition (16) will be fulfilled first upon increasing the coupling g_{MI} and thus either the majority or the impurity will form a shell. We remark that the above criterion for barrier formation is inversely proportional to the particle number of the other component, while the dependence on the trap ratio η for the majority differs substantially from the one for the impurity. Furthermore, for a fixed particle-number ratio there is a critical trap ratio η_c, for which (15) and (16) can be fulfilled simultaneously:

$$\sqrt{1/\eta_c} = \sqrt[7]{N_I/N_M}. \tag{17}$$

Around this critical region we expect that none of the components will occupy the trap center. We summarize our findings in a simple formula, which determines the type of phase separation at the miscible-immiscible phase boundary:

$$\begin{cases} \text{core shell } MIM & : \eta \gg \eta_c, \\ \text{core shell } IMI & : \eta \ll \eta_c, \\ CF \text{ or } SB & : \eta \approx \eta_c. \end{cases} \tag{18}$$

For particle-number ratios discussed in this section, the critical region lies at $a_I/a_M \approx 0.8$ [Fig. 1(a)] and at $a_I/a_M \approx 0.9$ [Fig. 1(b)].

Next, we want to find an estimate for the miscible-immiscible phase boundary g_{MI}^c. To this end, we combine the energetical separation criterion in Eq. (11) with approximate effective potentials from (13) and (14). Specifically, for a given particle number ratio N_I/N_M we determine the critical trap ratio η_c. Then depending on the choice of η we solve numerically for the ground-state energy of a single particle inside the effective potential (13) or (14). Finally, we compare this energy to the potential height at the trap center:

$$\begin{cases} a_I/a_M < \sqrt[7]{N_I/N_M} & : H_M^{\text{eff}} = -\dfrac{1}{2}\dfrac{\partial^2}{\partial x^2} + V_M^{\text{eff}}(x) \begin{cases} E_{0,M}^{\text{eff}} > g_{MI} N_I \sqrt{\frac{\eta}{\pi}} & \Rightarrow M, \\ E_{0,M}^{\text{eff}} < g_{MI} N_I \sqrt{\frac{\eta}{\pi}} & \Rightarrow MIM, \end{cases} \\ \\ a_I/a_M > \sqrt[7]{N_I/N_M} & : H_I^{\text{eff}} = -\dfrac{1}{2}\dfrac{\partial^2}{\partial y^2} + V_I^{\text{eff}}(y) \begin{cases} E_{0,I}^{\text{eff}} > g_{MI} N_B \sqrt{\frac{1}{\pi}} & \Rightarrow M, \\ E_{0,I}^{\text{eff}} < g_{MI} N_B \sqrt{\frac{1}{\pi}} & \Rightarrow IMI. \end{cases} \end{cases} \tag{19}$$

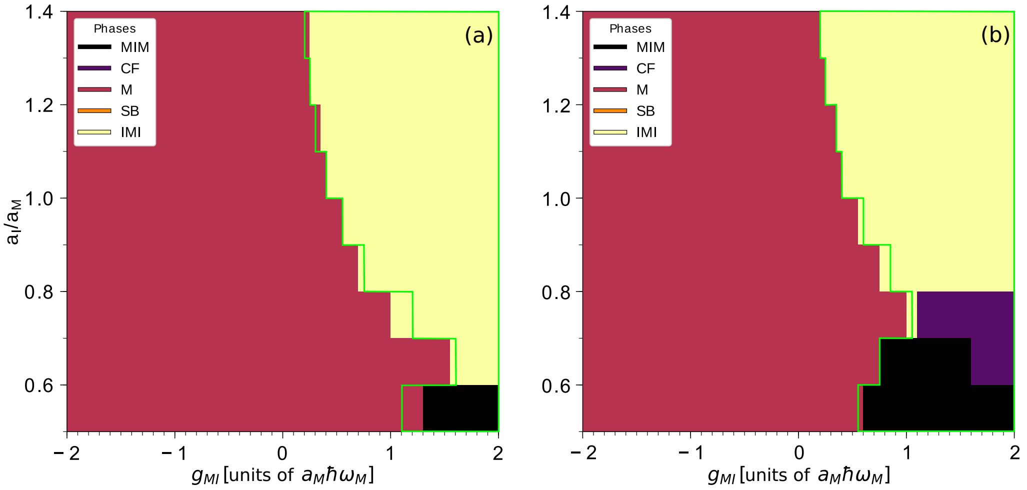

FIG. 3. ML-X ground-state phase diagram for $N_B = 5$ majority particles and (a) $N_I = 1$ or (b) $N_I = 2$ impurities as a function of the intercomponent coupling strength g_{MI} and impurity localization $a_I/a_M = \sqrt{1/\eta}$ with $\eta = \omega_I/\omega_M$ being the trap frequency ratio and $a_\sigma = \sqrt{\hbar/m\omega_\sigma}$ the harmonic oscillator length of species σ. The nomenclature of phases is as follows: *M* for miscible, *MIM* for core shell with impurity at the core, *IMI* for core shell with majority at the core, *CF* for composite fermionization, and *SB* for a phase with broken parity symmetry. The green solid curve represents the miscible-immiscible phase boundary based on the mean-field treatment. The coarse structure is due to the finite step size of our data with respect to a_I/a_M.

The results are plotted as blue solid curves in Fig. 1. We recognize that it performs quite well except for $\eta \approx \eta_c$, where it underestimates g_{MI}^c.

We can also get a rough estimate on the *SB* phase boundary g_{MI}^{SB} by using the following Gaussian ansatz:

$$\varphi^\sigma(z) = \sqrt[4]{\frac{\beta_\sigma}{\pi}}\, e^{-\frac{\beta_\sigma (z-z_\sigma)^2}{2}}, \tag{20}$$

with the width β_σ and the displacement z_σ of component σ being variational parameters. We evaluate the expectation value of (1) and minimize the energy with respect to the above variation parameters. By looking further at the special case when the relative position $|z_M - z_I|$ becomes zero, one arrives after some algebraic transformations at

$$g_{MI}^{SB} N_I = \frac{\sqrt{\pi}}{2\eta}\sqrt[4]{\frac{\gamma}{1+\gamma\eta^2}}\,(1+\eta^2\sqrt{\gamma})^{\frac{3}{2}}, \tag{21}$$

with particle-number ratio $\gamma = N_I/N_M$. We remark that this equation reduces to Eq. (8) from [60] for $\eta = 1$. Although this equation describes well the qualitative behavior of the *SB* phase boundary, quantitatively it scales badly when the trap ratio η deviates from η_c (blue dotted line in Fig. 1). There are two possible reasons for this. First, our ansatz incorporates only *M* and *SB* phases, while ignoring the core-shell phases. Thus, as one draws away from η_c the core-shell parameter region, which lies in-between *M* and *SB*, grows in size, making the estimate inefficient. The other reason is that the mean-field solution $\varphi_{\mathrm{MF}}^\sigma$ of the *SB* phase is rather an asymmetric Gaussian.

Finally, we discuss the limiting cases. When $\eta \to \infty$ ($a_I/a_M \to 0$) the impurity becomes highly localized at $z = 0$. It will not be affected by the majority atoms. Meanwhile, the majority species will be subject to an additional delta potential at $z = 0$ with potential strength $g_{MI}N_I$. This analytically solvable one-body problem results in a Weber differential equation. Upon increasing the delta-potential prefactor $g_{MI}N_I$, the initially unperturbed Gaussian solution develops a cusp at the trap center, whose depth tends to zero as the prefactor goes to infinity. When $\eta \to 0$ ($a_I/a_M \to \infty$), we can change our perspective by rescaling the Hamiltonian in impurity harmonic units and argue in a similar way as above.

In the following section, we compare to the results obtained for the corresponding correlated many-body approach of ML-X.

B. ML-X: Modifications of the phase diagram due to correlations and entanglement

For the total wave function in Eq. (2) we use $S = 8$ species orbitals and $s_\sigma = 8$ SPFs for each component. We perform again an imaginary-time propagation of an initially chosen wave function and obtain the ground state of (1). In Fig. 3 we show the resulting ground-state phases based on the selection rules (10) for $N_B = 5$ and (a) $N_I = 1$ or (b) $N_I = 2$. We remark that the alternative selection scheme defined in Eq. (11) does not apply here, and below we provide an explanation why it fails. The first eye-catching feature is that the *SB* phase has completely disappeared, as expected, since it is an artifact of the mean-field treatment. Additionally, we observe the presence of composite fermionization *CF* for the case of two impurities in Fig. 3(b). Overall, the transition between the miscible phase and separated phases takes places at a different coupling strength g_{MI}^c for a fixed trap ratio η.

In order to better understand why the phase diagram is altered this way, we investigate in Figs. 4 and 5 the von Neumann entropy S_{vN} on the species layer as well as the von Neumann entropy of the majority species S_{vN}^M and the impurity species S_{vN}^I. S_{vN} characterizes the degree of entanglement between the components (entanglement entropy) while S_{vN}^σ

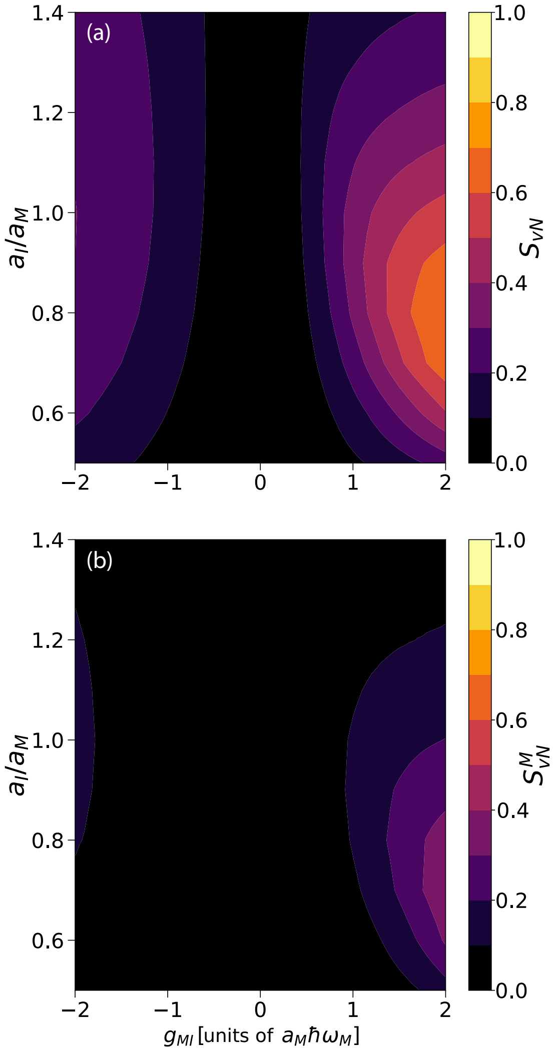

FIG. 4. Ground-state (species) entanglement entropy S_{vN} (a) from Eq. (22) and the fragmentation entropy S^M_{vN} from Eq. (23) for the majority (b) for $N_B = 5$ majority particles and $N_I = 1$ as a function of the intercomponent coupling strength g_{MI} and impurity localization $a_I/a_M = \sqrt{1/\eta}$ with $\eta = \omega_I/\omega_M$ being the trap frequency ratio and $a_\sigma = \sqrt{\hbar/m\omega_\sigma}$ the harmonic oscillator length of species σ.

reflects the degree of species fragmentation (fragmentation entropy). The definitions are as follows:

$$S_{vN} = -\sum_{i=1}^{S} \lambda_i \ln \lambda_i, \tag{22}$$

$$S^\sigma_{vN} = -\sum_{i=1}^{s_\sigma} m^\sigma_i \ln m^\sigma_i \quad \text{with } \hat{\rho}^\sigma_1 = \sum_{i=1}^{s_\sigma} m^\sigma_i \left|m^\sigma_i\right\rangle\left\langle m^\sigma_i\right|, \tag{23}$$

where λ_i are expansion coefficients from (2) and m^σ_i natural populations satisfying $\sum_{i=1}^{s_\sigma} m^\sigma_i = 1$ and $|m^\sigma_i\rangle$ natural orbitals of the spectrally decomposed one-body density operator $\hat{\rho}^\sigma_1$ of species σ. The entanglement entropy is bounded by the equal distribution of orbitals $S_{vN} \leqslant \ln(S)$, whereas for two dominantly occupied orbitals we expect $S_{vN} \leqslant \ln(2) \approx 0.7$. If $S_{vN} = 0$, then there is no entanglement between the species

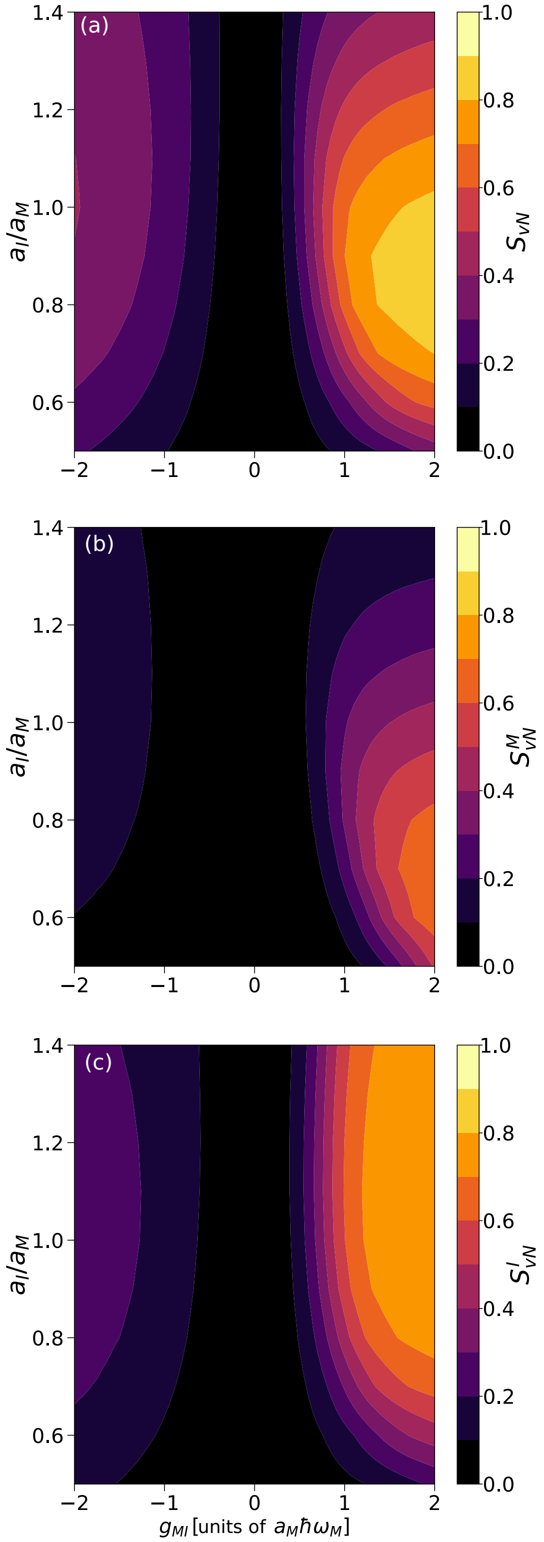

FIG. 5. Ground-state (species) entanglement entropy S_{vN} from Eq. (22) (a) and the fragmentation entropy S^σ_{vN} from Eq. (23) for the majority (b) and impurity (c) for $N_B = 5$ majority particles and $N_I = 2$ impurities as a function of the intercomponent coupling strength g_{MI} and impurity localization $a_I/a_M = \sqrt{1/\eta}$ with $\eta = \omega_I/\omega_M$ being the trap frequency ratio and $a_\sigma = \sqrt{\hbar/m\omega_\sigma}$ the harmonic oscillator length of species σ.

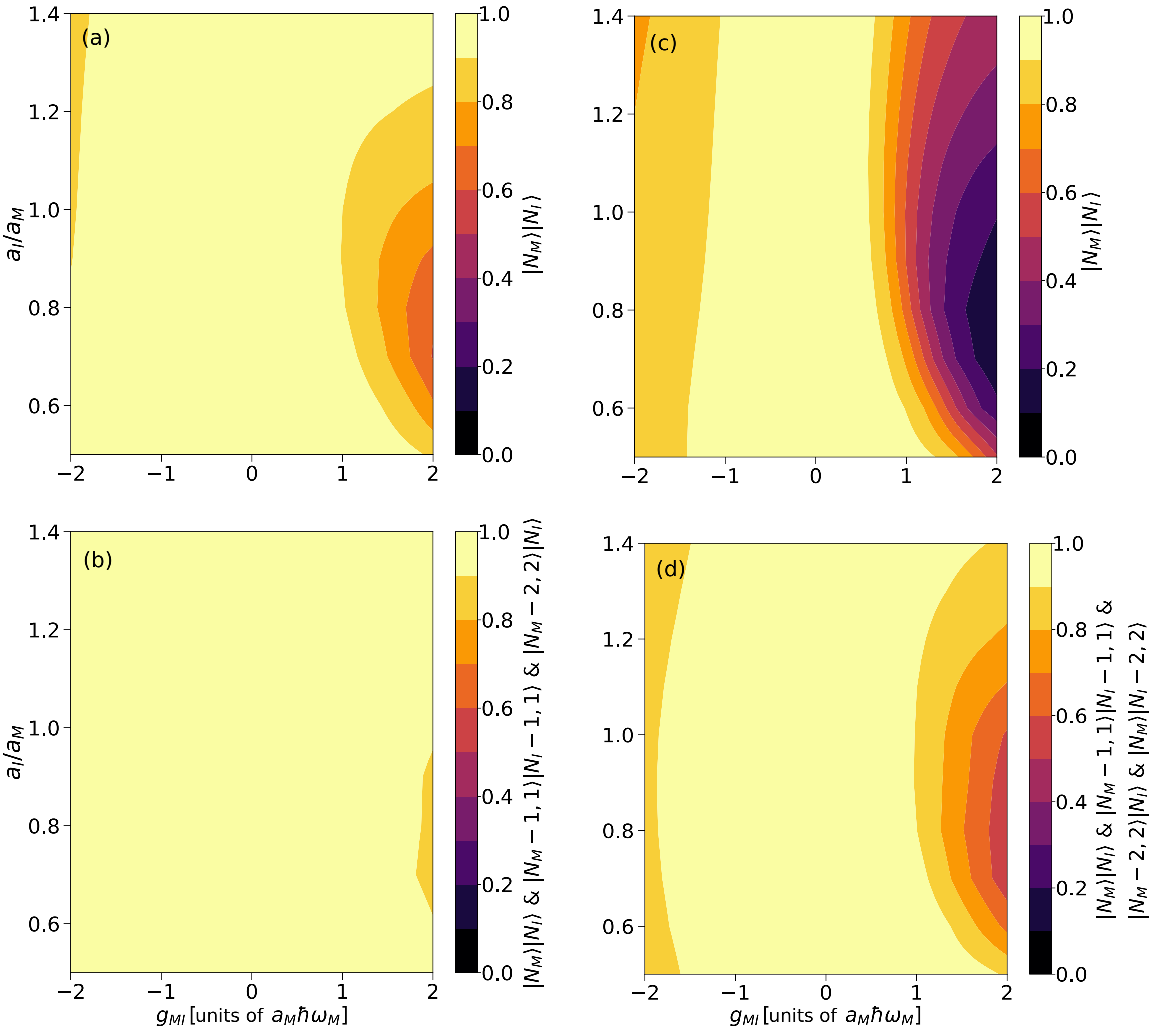

FIG. 6. Projection amplitudes of the many-body ground state on number states $|\langle\vec{n}^M|\otimes\langle\vec{n}^I||\Psi\rangle|^2$ for $N_B=5$ majority particles and $N_I=1$ (first column) or $N_I=2$ (second column) impurities as a function of the intercomponent coupling strength g_{MI} and impurity localization $a_I/a_M=\sqrt{1/\eta}$ with $\eta=\omega_I/\omega_M$ being trap frequency ratio and $a_\sigma=\sqrt{\hbar/m\omega_\sigma}$ the harmonic oscillator length of species σ. The SPFs constituting the permanents are eigenfunctions of the effective Hamiltonian (24). The first row corresponds to the projection on the condensed number state $|N_B\rangle\,|N_I\rangle$, while in the second row one sums over contributions from two-particle excitations $|N_B-2,2\rangle\,|N_I\rangle$, $|N_B\rangle\,|N_I-2,2\rangle$, and $|N_B-1,1\rangle\,|N_I-1,1\rangle$.

and the wave function is a simple product state on the species layer. Similarly, fragmentation entropy $S^\sigma_{vN}=0$ means that all particles occupy the same SPF and the species is thus condensed. For parameter values where this is fulfilled, a mean-field treatment is well justified. However, in Figs. 4 and 5 we recognize that for stronger couplings g_{MI} this is not the case. Particularly, in the vicinity of the critical region $a_I/a_M\approx\sqrt[7]{N_I/N_M}$ at positive g_{MI}, identified in the previous section as highly competitive, the entanglement entropy S_{vN} is very pronounced [Figs. 4(a) and 5(a)] . The fragmentation entropy of the majority species S^M_{vN} is comparatively weaker and slightly shifted toward a smaller length scale ratio a_I/a_M at positive g_{MI} [Figs. 4(b) and 5(b)]. The fragmentation entropy of the impurity species S^I_{vN} for $N_I=1$ (not shown) coincides with the entanglement entropy S_{vN} [Fig. 4(a)], while for $N_I=2$ there are substantial differences [see Fig. 5(c)]. Namely, the impurity shows a higher degree of fragmentation when it is less confined compared to the majority species and vice versa. In contrast to positive couplings g_{MI}, for negative couplings the entanglement and species fragmentation build up with a much slower rate. Finally, we emphasize that phase separations like core shell *MIM* or *IMI* are not necessarily related to a high degree of entanglement or species depletion, whereas *CF* is located in the parameter region, where S_{vN} takes the highest values. Another striking observation is that the onset of the *SB* phase from Fig. 1 is related to the entanglement entropy reaching some threshold value around $S_{vN}\approx 0.5$ at positive couplings g_{MI} [compare to Figs. 4(a) and 5(a)].

Now that we have identified the parameter space where deviations from mean field are to be expected, we want to gain a deeper insight into how the effective picture is affected as a result of increasing correlations. For this purpose we define an effective single-body Hamiltonian of species σ similar to the one in Eq. (7), except that we use the exact many-body

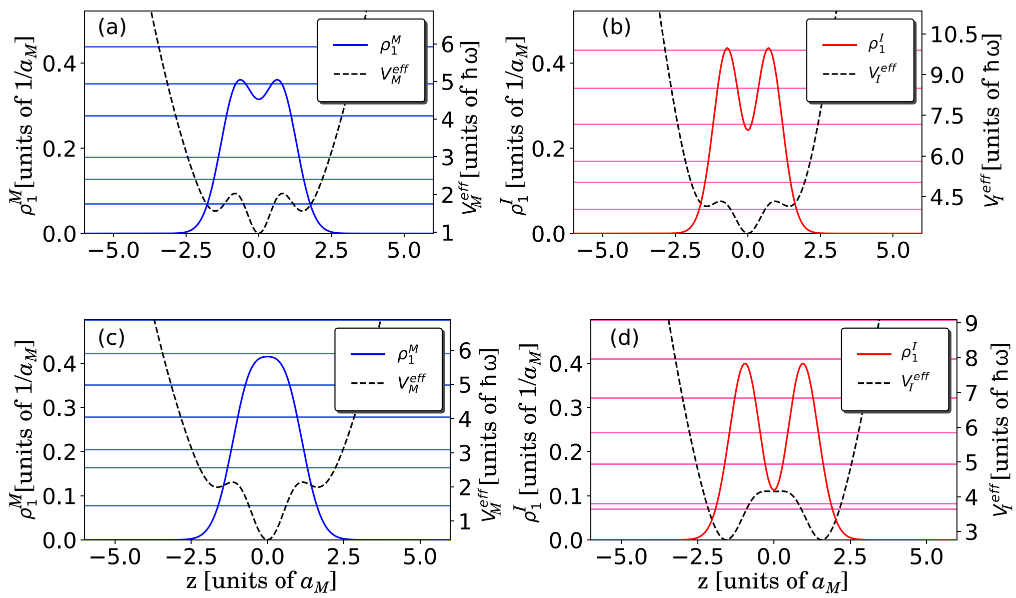

FIG. 7. ML-X ground-state densities $\rho_1^\sigma(z)$ inside effective one-body potentials $V_\sigma^{\text{eff}}(z)$ from (24) for $N_M = 5$, $N_I = 2$, $g_{MI} = 2$, and $a_I/a_M = 0.8$ (first row) or $a_I/a_M = 0.9$ (second row). Horizontal lines are eigenenergies of (24).

densities ρ_1^σ instead of the mean-field densities ρ_{MF}^σ:

$$H_\sigma^{\text{eff}} = H_\sigma + N_{\bar\sigma} g_{MI} \sum_{i=1}^{N_\sigma} \rho_1^{\bar\sigma}(z_i) \quad \text{with}$$

$$\bar\sigma \neq \sigma = \sum_{i=1}^{N_\sigma} \left(-\frac{1}{2} \frac{\partial^2}{\partial z_i^2} + V_\sigma^{\text{eff}}(z_i) \right). \qquad (24)$$

Next, we diagonalize (24) and use the obtained eigenfunctions $\tilde\varphi_i^\sigma$ as SPFs for number states $|\vec{n}^M\rangle \otimes |\vec{n}^I\rangle$ on which we project our many-body ground state $|\Psi\rangle$. The reader should distinguish the latter SPFs $\tilde\varphi_i^\sigma$ from the numerical SPFs φ_i^σ obtained by improved relaxation which define the permanents contained in our ML-X total wave function. Thus, we decompose our ground state in terms of disentangled product states made out of single permanents. We anticipate that $|N_M\rangle\,|N_I\rangle$ represents dominant contribution to $|\Psi\rangle$, which should be the case whenever a mean-field approach is valid. From the previous analysis we observed that the entanglement entropy values were mostly $S_{vN}^\sigma \leqslant 0.7$, which suggests two relevant SPFs. Indeed, our many-body state consists of two major orbitals and two major SPFs. Furthermore, taking parity symmetry into account and considering at most two-particle excitations, we conclude that number states $|N_M - 1, 1\rangle\,|N_I - 1, 1\rangle$, $|N_M - 2, 2\rangle\,|N_I\rangle$, and $|N_M\rangle\,|N_I - 2, 2\rangle$ may become of relevance too at stronger couplings. We remark that the one-body density operator of number state $|N_\sigma - n_2^\sigma, n_2^\sigma\rangle$ with n_2^σ particles in the odd orbital $\tilde\varphi_2^\sigma$ will be a mixed state of one even and one odd orbital, eventually featuring two humps in the corresponding one-body density. Thus, depending on the occupation amplitude of such states, they may either accelerate or slow down the development of humps in $\rho_1^\sigma(z)$, thereby quantitatively shifting the critical coupling g_{MI}^c, at which the mixed phase transforms into one of the species-separated phases.

In Fig. 6 we show the projection on number state $|N_M\rangle\,|N_I\rangle$ (first row) and a sum over projections on the above-mentioned permanents (second row) for $N_B = 5$ and $N_I = 1$ (first column) or $N_I = 2$ (second column). For negative couplings the state $|N_M\rangle\,|N_I\rangle$ provides a major contribution and the effective picture holds. Let us focus in the following on positive couplings. In Fig. 6(a) ($N_I = 1$), we observe that the state $|N_M\rangle\,|N_I\rangle$ has indeed a major contribution at coupling strength below 1.0. Once interspecies correlations build up with increasing coupling strength, the state $|N_M - 1, 1\rangle\,|N_I - 1, 1\rangle$ grows in importance, which corresponds to a simultaneous single-particle excitation within each component. This is mostly pronounced around η_c. Double excitations within the majority species $|N_M - 2, 2\rangle\,|N_I\rangle$ are of minor amplitude and rather of relevance for a localized impurity $a_I/a_M \ll 1$. All in all, the low-lying excitations of the effective potentials (24) provide a good description [Fig. 6(b)]. In Fig. 6(c) ($N_I = 2$), we observe that the state $|N_M\rangle\,|N_I\rangle$ loses its contribution very quickly as one goes deeper into the regime of strong entanglement. Although we are able to get a better understanding for weak entanglement by including two-particle excitations mentioned above, our effective picture clearly does not hold in the parameter region characterized by strong entanglement. There, we may account only for as much as ≈50% of the ground state, even though the one-body density in Eq. (24) incorporates beyond-mean-field corrections. We remark that while it is indeed intuitive that the one-body picture will break at some point as the entanglement becomes stronger, it is not at all obvious to predict the corresponding threshold (trap ratio and coupling strength) where it will happen.

Let us take a closer look at this regime, where the single-particle picture (24) tends to break down. We show in Fig. 7 the one-body densities for $N_B = 5$ majority particles and $N_I = 2$ impurities in the strong entanglement region at $g_{MI} = 2$. The first row corresponds to the *CF* phase at $a_I/a_M = 0.8$. Here, we recognize immediately why the effective picture fails. The origin of the two humps in the one-body density is counterintuitive considering that they are at the position of local maxima of the effective potential. One would rather

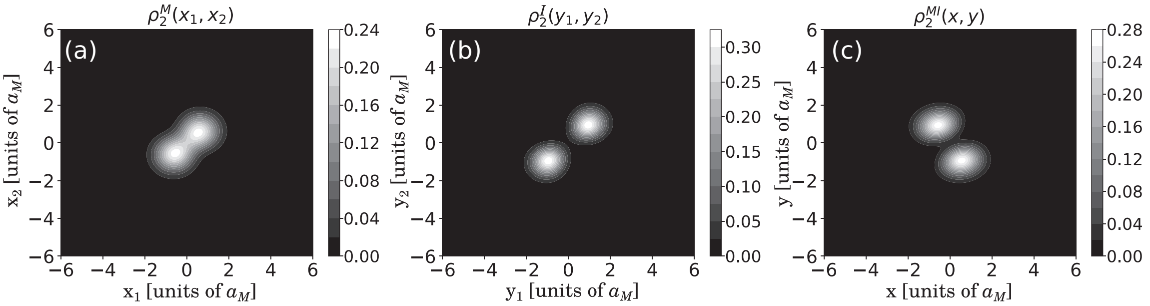

FIG. 8. (a) Majority two-body density matrix $\rho_2^M(x_1,x_2)$ from Eq. (5). (b) Impurity two-body density matrix $\rho_2^I(y_1,y_2)$ from Eq. (5). (c) Interspecies two-body density matrix $\rho_2^{MI}(x,y)$ from Eq. (6) of the ground state for $N_M=5$, $N_I=2$, $g_{MI}=2$, and $a_I/a_M=0.9$.

expect a density profile with three peaks at the positions of the potential minima.

The second row ($a_I/a_M=0.9$) seems at first glance to be an *IMI* phase. The majority is at the core, while the impurity forms a shell. Upon a more detailed investigation we notice that the majority species is broader than it should be inside the squeezed "harmonic" trap. The humps of the impurity also do not coincide with the positions of the minima of the respective effective potential. As a matter of fact, this phase is a latent *CF* phase, which becomes clear when we analyze the corresponding two-body density matrices in Fig. 8. The intraspecies two-body density matrices (5) [Figs. 8(a) and 8(b)] indicate that particles of the same component avoid the trap center and form a cluster either on the right or the left side with respect to trap center. Moreover, the interspecies density matrix (6) [Fig. 8(c)] tells us that the two different clusters of majority and impurity will always be found on opposite sides of the trap with a rather small spatial overlap between them. It allows to diminish the impact of the repulsive energy on the total energy at the cost of paying potential energy. These are clear signatures of the *CF*, which are blurred in the reduced one-body density. We note that the parameter space where ML-X predicts an *IMI* phase, whereas MF produces *SB* phase, we have in fact a latent *CF*, hidden behind a one-body quantity. Thus, in general, the classification of immiscible phases by the one-body density is not sufficient to distinguish *CF* from *IMI* or *MIM*. Nevertherless, sometimes it is still possible to identify *CF* by the one-body density, namely, when it features two reflection-symmetric humps.

Above, we have mentioned that in the literature the *CF* phase was suggested to be a superposition of two parity-broken mean-field states $|\Psi\rangle = c_1\,|N_M\rangle_L\,|0_M\rangle_R \otimes |0_I\rangle_L\,|N_I\rangle_R + c_2\,|0_M\rangle_L\,|N_M\rangle_R \otimes |N_I\rangle_L\,|0_I\rangle_R$ as a result of the degeneracy onset. Indeed, ML-X has two prominent orbitals on the species layer and two major SPFs on the particle layer. Nevertheless, the other occupied species orbitals and SPFs provide a minor contribution, as we have evidenced in Fig. 5, where the entropies take values beyond ln(2). To provide an illustrative example, we displace the trap centers in Eq. (1) by a small amount to energetically separate the two symmetry-broken configurations. For parameter values for which the *CF* phase is observed, we perform again the improved relaxation to the find ground state of the system in order to check whether it is indeed a MF state. It turns out that the majority species and the impurity species are still fragmented states though the degree of depletion is much less compared to the parity-symmetric ground state. The species entropy S_{vN} is greatly reduced, but still appreciable. The impact of correlations is also visible in Fig. 9. The ground state of the effective potential (24) is different from the one-body density of the many-body ML-X wave function. This is caused by induced attractive interactions mediated by the intercomponent coupling, a beyond-mean-field effect [92].

To conclude our discussion about the high-entanglement regime, we state that the mean-field approach, being an effective one-body model, fails to explain a one-body quantity such as reduced one-body density. Nevertheless, it manages to characterize quite well one of the two possible configurations of the entangled many-body state. The latter is not just a simple superposition of two mean-field states describing two different parity-broken configurations. A thorough analysis showed that on the many-body level the *SB* phase is in fact

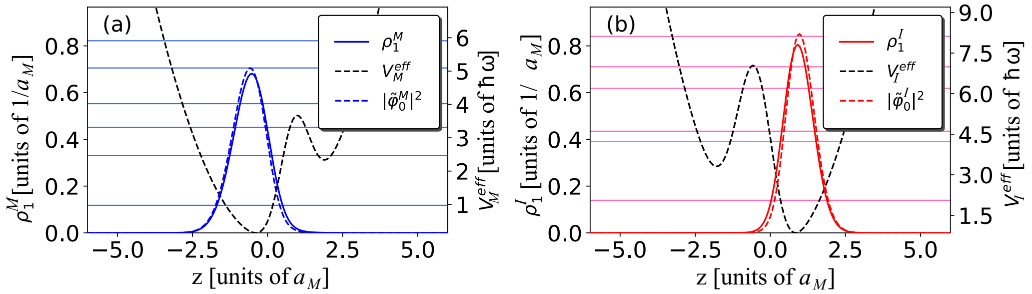

FIG. 9. ML-X parity-broken ground-state densities $\rho_1^\sigma(z)$ obtained from (1) by slightly displacing centers of harmonic traps in opposite directions for $N_M=5$, $N_I=2$, $g_{MI}=2$, and $a_I/a_M=0.9$. Induced one-body potentials $V_\sigma^{\mathrm{eff}}(z)$ are calculated from (24) and $\tilde{\varphi}_0^\sigma(z)$ are the corresponding ground states. Horizontal lines are eigenenergies of (24).

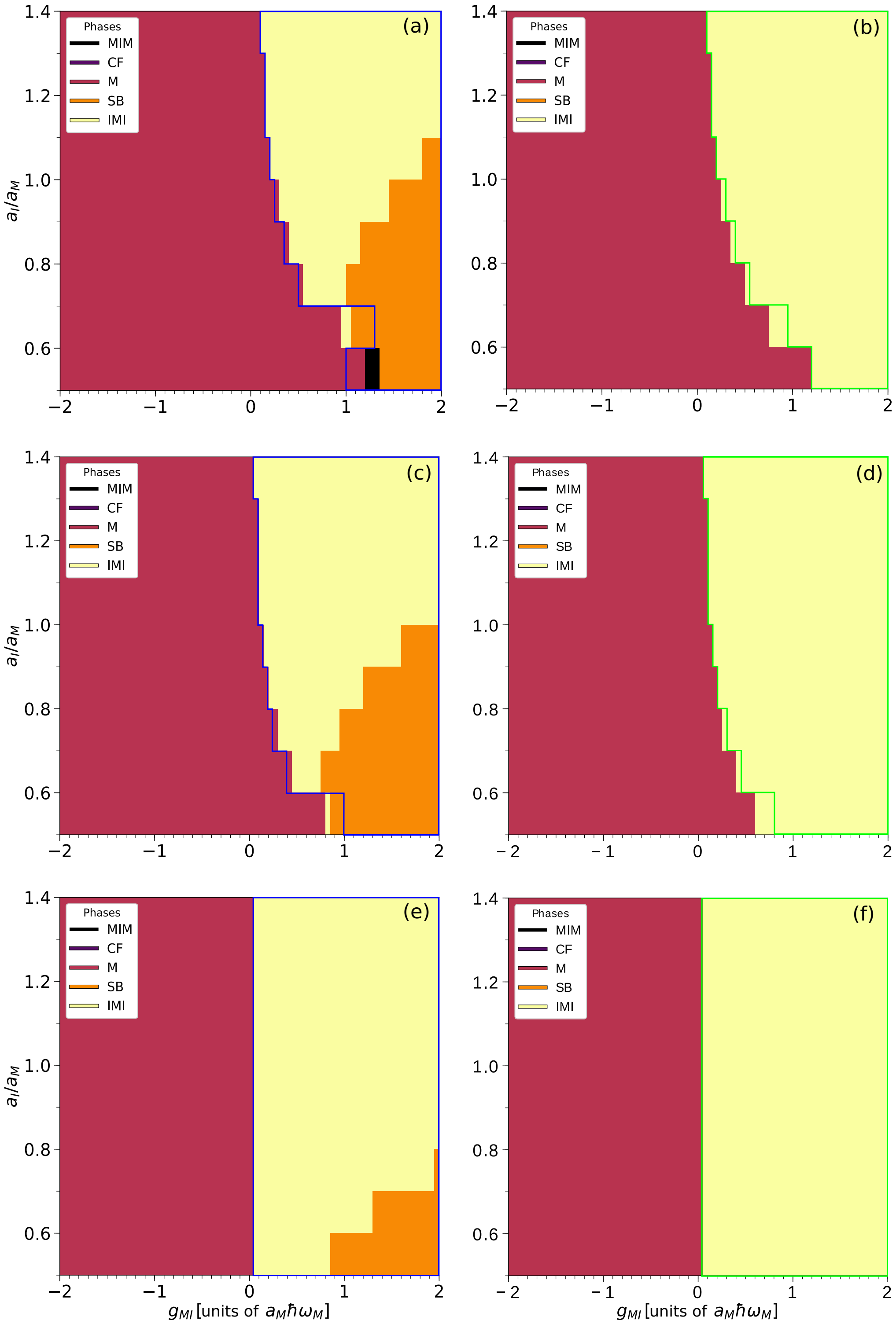

FIG. 10. Mean-field (first column) and ML-X (second column) ground-state phase diagrams for $N_I = 1$ impurity and $N_M = 10$ (first row), $N_M = 20$ (second row), or $N_M = 1000$ (third row) as a function of the intercomponent coupling strength g_{MI} and impurity localization $a_I/a_M = \sqrt{1/\eta}$ with $\eta = \omega_I/\omega_M$ being the trap frequency ratio and $a_\sigma = \sqrt{\hbar/m\omega_\sigma}$ the harmonic oscillator length of species σ. The nomenclature of the phases is as follows: M for miscible, MIM for core shell with impurity at the core, IMI for core shell with majority at the core, CF for composite fermionization, and SB for a phase with broken parity symmetry. The blue solid curve (first column) represents the miscible-immiscible phase boundary according to (19). The green solid curve (second column) is the miscible-immiscible phase boundary based on mean field. The coarse structure is due to the finite step size of our data with respect to a_I/a_M.

slightly entangled, while each species is partially fragmented. We also evidenced that *CF* completely dominates the highly correlated regime and made a link of its appearance to the onset of *SB* on the mean-field level. Sometimes, *CF* is even camouflaged behind core-shell *IMI* or *MIM* densities, indicating that the one-body density is not enough to distinguish between them.

V. PHASE SEPARATION: IMPACT OF PARTICLE NUMBERS

When increasing the number of majority atoms N_M, while keeping N_I fixed, one might expect two properties based on an intuition for few-body systems. First, the location of the strong entanglement regime will be shifted toward lower values of $a_I/a_M \approx \sqrt{1/\eta_c} = \sqrt[7]{N_I/N_M}$. Thus, the *IMI* phase will cover the most part of our parameter space for positive g_{MI}. Second, at a fixed η the critical coupling g_{MI}^c for the miscible-immiscible transition will decrease, because according to (16) the majority species will be able to induce a barrier for the impurity species already for a much weaker coupling. The induced barrier of the majority on the other hand will not be affected according to (15).

Indeed, this is what we observe in the phase diagrams depicted in Fig. 10. In the mean field (first column) the location of the *SB* phase relocates from $\sqrt{1/\eta_c} \approx 0.79$ [$N_M = 5$, Fig. 1(a)] to $\sqrt{1/\eta_c} \approx 0.72$ [$N_M = 10$, Fig. 10(a)], then to $\sqrt{1/\eta_c} \approx 0.65$ [$N_M = 20$, Fig. 10(b)] and finally moves outside our parameter space $\sqrt{1/\eta_c} \approx 0.37$ [$N_M = 1000$, Fig. 10(c)]. The blue curve, which estimates the miscible-immiscible transition according to (19) is in good agreement (except for the critical region η_c) with the mean-field phase boundary. We also recognize that for a fixed trap ratio η, the critical coupling strength g_{MI}^c decreases with increasing N_M and at $N_M = 1000$ a very small $g_{MI}^c < 0.05$ is sufficient to cause phase separation, which is below our resolution.

We have also performed the corresponding ML-X calculations (second column) with $S = s_\sigma = 6$ (first row), $S = s_\sigma = 4$ (second row), and $S = s_\sigma = 2$ (third row) orbitals. We remark that the latter case might not be converged to the exact solution, which is beyond numerical capabilities to verify. Still, it provides valuable beyond-mean-field corrections. The deviations to the mean field, still clearly visible at $N_M = 10$, are most pronounced near η_c. They become less as the particle imbalance is increased until finally at $N_M = 1000$ the phase diagrams almost coincide except for a small *SB* region. This is mainly attributed to the fact that the strong entanglement regime, where deviations are to be expected, moves outside our parameter space ($a_I/a_M < 0.5$). Furthermore, the deviations may still be there, but on a finer coupling scale $g_{MI} < 0.05$ according to (15) and (16).

VI. CONCLUSIONS

In this work we have investigated the phase separation of a quasi-1D inhomogeneous Bose-Bose mixture in a three-dimensional parameter space spanned by the intercomponent coupling g_{MI}, harmonic length scale ratio $a_I/a_M = \sqrt{1/\eta}$, and the particle-number ratio N_I/N_M, when the intracomponent couplings g_σ are switched off. Although we have concentrated on the case of equal masses, our results may be easily extended to the more general case of unequal masses. We expect some quantitative changes, but the qualitative picture and the line of argumentation will remain unchanged.

The commonly used separation criterion $g_{MI} > \sqrt{g_M g_I}$, which is valid for homogeneous mixtures, would predict a miscible-immiscible transition for any finite coupling $g_{MI} > 0$. However, this separation rule does not apply here since we have harmonic traps of different length scales. We have analyzed the mechanism, which leads to phase separation, by using an effective mean-field picture. Within this description each species is subject to an additional induced potential caused by the other component. This potential has initially a Gaussian shape and grows linearly with the coupling strength g_{MI}. However, it does not immediately trigger a barrier at the center of the harmonic trap. In fact, the species, which first manages to induce a barrier for the other component upon increasing the coupling g_{MI}, will stay at the center of its parabolic trap. Meanwhile, the other species will split up, once the ground-state energy of the effective potential drops below the barrier height. Thus, we end up with either a core-shell *IMI* or a core-shell *MIM* phase, except for a highly competitive region, where the barrier conditions can be met simultaneously for both components. We have derived a simple rule to predict the type of phase separation, developed a straightforward algorithm to identify the miscible-immiscible phase boundary g_{MI}^c, and gave a rough estimate on the phase boundary between the segregated phases g_{MI}^{SB}.

As a next step, we compared mean-field (MF) results to the numerically exact many-body calculations based on multilayer multiconfigurational time-dependent Hartree method for atomic mixtures (ML-X). It turns out that MF agrees well with ML-X far away from the critical region $\sqrt{1/\eta_c} = \sqrt[7]{N_I/N_M}$. At η_c there are considerable quantitative deviations and sometimes the two methods do not even agree on the type of phase separation. This is caused by the growing interparticle correlations, which generate entanglement between the components and increase the degree of species fragmentation. We have seen that symmetry-broken phase (*SB*) is replaced by composite fermionization (*CF*), which is an entangled parity-symmetric ground state. Furthermore, we have linked the onset of *SB* to the fact that the entanglement entropy reaches a certain threshold and saw a clear breakdown of the effective single-particle picture in the strong entanglement region in terms of a corresponding number state analysis. This led to the discovery of a latent *CF* phase in the *IMI* region. The latent *CF* phase has the characteristic one-body density of the *IMI* phase, but a thorough analysis of the two-body densities reveals typical *CF* features. We have argued that at a finite coupling g_{MI} the *CF* is not a simple superposition of two *SB* states given by mean field.

We have studied the impact of particle-number variations, which confirmed our intuition that η_c and thus the location of the strong entanglement regime can be manipulated as a function of the particle-number ratio. Furthermore, for a fixed particle-number ratio the critical coupling g^c_{MI} of the miscible-immiscible transition can be tuned to lower values by increasing the number of particles while keeping the particle-number ratio fixed.

Finally, we remark that an intriguing next step would be to perform a similar study of phase separation at finite intracomponent coupling g_σ. The broadening or shrinking of the density profiles, depending on the sign and strength of g_σ, will definitely modify the barrier conditions (15) and (16). Another interesting but challenging direction would be the nonequilibrium dynamics by quenching the trap ratio across the phase boundaries.

ACKNOWLEDGMENTS

M.P. acknowledges fruitful discussions with K. Keiler and M. Roentgen. M.P. gratefully acknowledges a scholarship of the Studienstiftung des deutschen Volkes.

[1] R. Grimm, M. Weidemüller, and Y. B. Ovchinnikov, Adv. At. Mol. Opt. Phys. **42**, 95 (2000).

[2] I. Bloch, J. Dalibard, and W. Zwerger, Rev. Mod. Phys. **80**, 885 (2008).

[3] M. A. Cazalilla, R. Citro, T. Giamarchi, E. Orignac, and M. Rigol, Rev. Mod. Phys. **83**, 1405 (2011).

[4] C. Chin, R. Grimm, P. Julienne, and E. Tiesinga, Rev. Mod. Phys. **82**, 1225 (2010).

[5] M. Olshanii, Phys. Rev. Lett. **81**, 938 (1998).

[6] D. S. Petrov, M. Holzmann, and G. V. Shlyapnikov, Phys. Rev. Lett. **84**, 2551 (2000).

[7] T. Bergeman, M. G. Moore, and M. Olshanii, Phys. Rev. Lett. **91**, 163201 (2003).

[8] E. Haller, M. J. Mark, R. Hart, J. G. Danzl, L. Reichsöllner, V. Melezhik, P. Schmelcher, and H.-C. Nägerl, Phys. Rev. Lett. **104**, 153203 (2010).

[9] D. Blume, Rep. Prog. Phys. **75**, 046401 ’ (2012).

[10] T. Sowiński and M. Á. García-March, Rep. Prog. Phys. **82**, 104401 (2019).

[11] C. J. Myatt, E. A. Burt, R. W. Ghrist, E. A. Cornell, and C. E. Wieman, Phys. Rev. Lett. **78**, 586 (1997).

[12] D. S. Hall, M. R. Matthews, J. R. Ensher, C. E. Wieman, and E. A. Cornell, Phys. Rev. Lett. **81**, 1539 (1998).

[13] H.-J. Miesner, D. M. Stamper-Kurn, J. Stenger, S. Inouye, A. P. Chikkatur, and W. Ketterle, Phys. Rev. Lett. **82**, 2228 (1999).

[14] P. Maddaloni, M. Modugno, C. Fort, F. Minardi, and M. Inguscio, Phys. Rev. Lett. **85**, 2413 (2000).

[15] G. Delannoy, S. G. Murdoch, V. Boyer, V. Josse, P. Bouyer, and A. Aspect, Phys. Rev. A **63**, 051602(R) (2001).

[16] K. M. Mertes, J. W. Merrill, R. Carretero-González, D. J. Frantzeskakis, P. G. Kevrekidis, and D. S. Hall, Phys. Rev. Lett. **99**, 190402 (2007).

[17] S. Tojo, Y. Taguchi, Y. Masuyama, T. Hayashi, H. Saito, and T. Hirano, Phys. Rev. A **82**, 033609 (2010).

[18] C. Becker, S. Stellmer, P. Soltan-Panahi, S. Dörscher, M. Baumert, E.-M. Richter, J. Kronjäger, K. Bongs, and K. Sengstock, Nat. Phys. **4**, 496 (2008).

[19] C. Hamner, J. J. Chang, P. Engels, and M. A. Hoefer, Phys. Rev. Lett. **106**, 065302 (2011).

[20] E. Nicklas, M. Karl, M. Höfer, A. Johnson, W. Muessel, H. Strobel, J. Tomkovič, T. Gasenzer, and M. K. Oberthaler, Phys. Rev. Lett. **115**, 245301 (2015).

[21] Y. Eto, M. Takahashi, K. Nabeta, R. Okada, M. Kunimi H. Saito, and T. Hirano, Phys. Rev. A **93**, 033615 (2016).

[22] Y. Eto, M. Takahashi, M. Kunimi, H. Saito, and T. Hirano, New J. Phys. **18**, 073029 (2016).

[23] C. Cabrera, L. Tanzi, J. Sanz, B. Naylor, P. Thomas, P. Cheiney, and L. Tarruell, Science **359**, 301 (2018).

[24] G. Semeghini, G. Ferioli, L. Masi, C. Mazzinghi, L. Wolswijk, F. Minardi, M. Modugno, G. Modugno, M. Inguscio, and M. Fattori, Phys. Rev. Lett. **120**, 235301 (2018).

[25] G. Modugno, M. Modugno, F. Riboli, G. Roati, and M. Inguscio, Phys. Rev. Lett. **89**, 190404 (2002).

[26] M. Mudrich, S. Kraft, K. Singer, R. Grimm, A. Mosk, and M. Weidemüller, Phys. Rev. Lett. **88**, 253001 (2002).

[27] G. Thalhammer, G. Barontini, L. De Sarlo, J. Catani, F. Minardi, and M. Inguscio, Phys. Rev. Lett. **100**, 210402 (2008).

[28] K.-K. Ni, S. Ospelkaus, M. De Miranda, A. Pe’Er, B. Neyenhuis, J. Zirbel, S. Kotochigova, P. Julienne, D. Jin, and J. Ye, Science **322**, 231 (2008).

[29] D. J. McCarron, H. W. Cho, D. L. Jenkin, M. P. Köppinger, and S. L. Cornish, Phys. Rev. A **84**, 011603(R) (2011).

[30] A. D. Lercher, T. Takekoshi, M. Debatin, B. Schuster, R. Rameshan, F. Ferlaino, R. Grimm, and H. C. Nägerl, Eur. Phys. J. D **65**, 3 (2011).

[31] B. Pasquiou, A. Bayerle, S. M. Tzanova, S. Stellmer, J. Szczepkowski, M. Parigger, R. Grimm, and F. Schreck, Phys. Rev. A **88**, 023601 (2013).

[32] T. Takekoshi, L. Reichsöllner, A. Schindewolf, J. M. Hutson, C. R. Le Sueur, O. Dulieu, F. Ferlaino, R. Grimm, and H.-C. Nägerl, Phys. Rev. Lett. **113**, 205301 (2014).

[33] P. K. Molony, P. D. Gregory, Z. Ji, B. Lu, M. P. Köppinger, C. R. Le Sueur, C. L. Blackley, J. M. Hutson, and S. L. Cornish, Phys. Rev. Lett. **113**, 255301 (2014).

[34] L. Wacker, N. B. Jørgensen, D. Birkmose, R. Horchani, W. Ertmer, C. Klempt, N. Winter, J. Sherson, and J. J. Arlt, Phys. Rev. A **92**, 053602 (2015).

[35] X. Li, B. Zhu, X. He, F. Wang, M. Guo, Z.-F. Xu, S. Zhang, and D. Wang, Phys. Rev. Lett. **114**, 255301 (2015).

[36] K. L. Lee, N. B. Jørgensen, L. J. Wacker, M. G. Skou, K. T. Skalmstang, J. J. Arlt, and N. P. Proukakis, New J. Phys. **20**, 053004 (2018).

[37] F. Wang, X. Li, D. Xiong, and D. Wang, J. Phys. B. At. Mol. Phys. **49**, 015302 (2015).

[38] G. Barontini, C. Weber, F. Rabatti, J. Catani, G. Thalhammer, M. Inguscio, and F. Minardi, Phys. Rev. Lett. **103**, 043201 (2009).

[39] S. B. Papp, J. M. Pino, and C. E. Wieman, Phys. Rev. Lett. **101**, 040402 (2008).

[40] S. Sugawa, R. Yamazaki, S. Taie, and Y. Takahashi, Phys. Rev. A **84**, 011610(R) (2011).

[41] K. Kasamatsu and M. Tsubota, Phys. Rev. Lett. **93**, 100402 (2004).

[42] S. Ronen, J. L. Bohn, L. E. Halmo, and M. Edwards, Phys. Rev. A **78**, 053613 (2008).

[43] H. Takeuchi, S. Ishino, and M. Tsubota, Phys. Rev. Lett. **105**, 205301 (2010).

[44] J. Hofmann, S. S. Natu, and S. Das Sarma, Phys. Rev. Lett. **113**, 095702 (2014).

[45] K. Kasamatsu, M. Tsubota, and M. Ueda, Phys. Rev. Lett. **91**, 150406 (2003).

[46] P. Mason and A. Aftalion, Phys. Rev. A **84**, 033611 (2011).

[47] T.-L. Ho and V. B. Shenoy, Phys. Rev. Lett. **77**, 3276 (1996).

[48] H. Pu and N. P. Bigelow, Phys. Rev. Lett. **80**, 1130 (1998).

[49] A. A. Svidzinsky and S. T. Chui, Phys. Rev. A **67**, 053608 (2003).

[50] P. Öhberg, Phys. Rev. A **59**, 634 (1999).

[51] M. Trippenbach, K. Góral, K. Rzazewski, B. Malomed, and Y. Band, J. Phys. B. At. Mol. Phys. **33**, 4017 (2000).

[52] A. Alexandrov and V. V. Kabanov, J. Phys.: Condens. Matter **14**, L327 (2002).

[53] E. Timmermans, Phys. Rev. Lett. **81**, 5718 (1998).

[54] P. Ao and S. T. Chui, Phys. Rev. A **58**, 4836 (1998).

[55] B. D. Esry, C. H. Greene, J. P. Burke, Jr., and J. L. Bohn, Phys. Rev. Lett. **78**, 3594 (1997).

[56] R. Navarro, R. Carretero-González, and P. G. Kevrekidis, Phys. Rev. A **80**, 023613 (2009).

[57] L. Wen, W. M. Liu, Y. Cai, J. M. Zhang, and J. Hu, Phys. Rev. A **85**, 043602 (2012).

[58] K. L. Lee, N. B. Jørgensen, I.-K. Liu, L. Wacker, J. J. Arlt, and N. P. Proukakis, Phys. Rev. A **94**, 013602 (2016).

[59] V. Cikojević, L. V. Markić, and J. Boronat, New J. Phys. **20**, 085002 (2018).

[60] L. Wen, H. Guo, Y.-J. Wang, A.-Y. Hu, H. Saito, C.-Q. Dai, and X.-F. Zhang, Phys. Rev. A **101**, 033610 (2020).

[61] B. Parajuli, D. Pęcak, and C.-C. Chien, Phys. Rev. A **100**, 063623 (2019).

[62] F. Lingua, A. Richaud, and V. Penna, Entropy **20**, 84 (2018).

[63] G. M. Koutentakis, S. I. Mistakidis, and P. Schmelcher, New J. Phys. **22**, 063058 (2020).

[64] J. Erdmann, S. I. Mistakidis, and P. Schmelcher, Phys. Rev. A **99**, 013605 (2019).

[65] V. Penna and A. Richaud, Sci. Rep. **8**, 10242 (2018).

[66] A. Richaud, A. Zenesini, and V. Penna, Sci. Rep. **9**, 6908 (2019).

[67] K. Keiler and P. Schmelcher, New J. Phys. **20**, 103042 (2018).

[68] K. Keiler, S. I. Mistakidis, and P. Schmelcher, New J. Phys. (2020).

[69] S. Mistakidis, G. Katsimiga, P. Kevrekidis, and P. Schmelcher, New J. Phys. **20**, 043052 (2018).

[70] S. I. Mistakidis, L. Hilbig, and P. Schmelcher, Phys. Rev. A **100**, 023620 (2019).

[71] S. I. Mistakidis, G. C. Katsimiga, G. M. Koutentakis, T. Busch, and P. Schmelcher, Phys. Rev. Lett. **122**, 183001 (2019).

[72] S. Mistakidis, G. Koutentakis, G. Katsimiga, T. Busch, and P. Schmelcher, New J. Phys. **22**, 043007 (2020).

[73] S. Zöllner, H.-D. Meyer, and P. Schmelcher, Phys. Rev. A **78**, 013629 (2008).

[74] Y. J. Hao and S. Chen, Eur. Phys. J. D **51**, 261 (2009).

[75] M. A. García-March, B. Juliá-Díaz, G. Astrakharchik, T. Busch, J. Boronat, and A. Polls, New J. Phys. **16**, 103004 (2014).

[76] A. Dehkharghani, A. Volosniev, J. Lindgren, J. Rotureau, C. Forssén, D. Fedorov, A. Jensen, and N. Zinner, Sci. Rep. **5**, 10675 (2015).

[77] M. Pyzh, S. Krönke, C. Weitenberg, and P. Schmelcher, New J. Phys. **20**, 015006 (2018).

[78] F. Deuretzbacher, D. Becker, J. Bjerlin, S. M. Reimann, and L. Santos, Phys. Rev. A **90**, 013611 (2014).

[79] A. G. Volosniev, D. Petrosyan, M. Valiente, D. V. Fedorov, A. S. Jensen, and N. T. Zinner, Phys. Rev. A **91**, 023620 (2015).

[80] L. Yang and X. Cui, Phys. Rev. A **93**, 013617 (2016).

[81] L. Cao, S. Krönke, O. Vendrell, and P. Schmelcher, J. Chem. Phys. **139**, 134103 (2013).

[82] S. Krönke, L. Cao, O. Vendrell, and P. Schmelcher, New J. Phys. **15**, 063018 (2013).

[83] L. Cao, V. Bolsinger, S. Mistakidis, G. Koutentakis, S. Krönke, J. Schurer, and P. Schmelcher, J. Chem. Phys. **147**, 044106 (2017).

[84] L. J. LeBlanc and J. H. Thywissen, Phys. Rev. A **75**, 053612 (2007).

[85] A. Rubio-Abadal, J.-Y. Choi, J. Zeiher, S. Hollerith, J. Rui, I. Bloch, and C. Gross, Phys. Rev. X **9**, 041014 (2019).

[86] F. Serwane, G. Zürn, T. Lompe, T. Ottenstein, A. Wenz, and S. Jochim, Science **332**, 336 (2011).

[87] R. Islam, R. Ma, P. M. Preiss, M. E. Tai, A. Lukin, M. Rispoli, and M. Greiner, Nature (London) **528**, 77 (2015).

[88] M. Pyzh, S. Krönke, C. Weitenberg, and P. Schmelcher, New J. Phys. **21**, 053013 (2019).

[89] M. H. Beck, A. Jäckle, G. A. Worth, and H.-D. Meyer, Phys. Rep. **324**, 1 (2000).

[90] J. Light, I. Hamilton, and J. Lill, J. Chem. Phys. **82**, 1400 (1985).

[91] A. Raab, Chem. Phys. Lett. **319**, 674 (2000).

[92] J. Chen, J. M. Schurer, and P. Schmelcher, Phys. Rev. Lett. **121**, 043401 (2018).